J Mater Sci: Mater Electron

Effect of A-site off-stoichiometry on the microstructural, structural, and electromechanical properties of lead-free tetragonal $0.80Na_{0.5}Bi_{0.5}TiO_3$–$0.20BaTiO_3$ (NBT–20BT) piezoceramic

Anupam Mishra[1,*], Getaw Abebe[1,2], Gudeta Jafo[1,2], Gobinda Das Adhikary[1], and Arnab De[1]

[1] Department of Materials Engineering, Indian Institute of Science, Bangalore 560012, India
[2] Faculty of Materials Science and Engineering, Jimma Institute of Technology, Jimma, Ethiopia

Received: 25 January 2021
Accepted: 1 April 2021

© The Author(s), under exclusive licence to Springer Science+Business Media, LLC, part of Springer Nature 2021

ABSTRACT

A-site off-stoichiometry has been an efficient method to enhance the electromechanical properties of lead-free $Na_{0.5}Bi_{0.5}TiO_3$(NBT)-based piezoceramics. In this work, we have reported the effect of Na/Bi off-stoichiometry on the microstructural, structural, and electromechanical properties of the tetragonal $0.80Na_{0.5}Bi_{0.5}TiO_3$–$0.20BaTiO_3$ (NBT–20BT) ceramic. The maximum piezoresponse ~ 115 pC/N is obtained for 4 mol% Na-deficient (20BT–Na46) and 2 mol% Bi-excess (20BT–Bi52) compositions. It is a 25% increment over the piezoresponse of the stoichiometric composition (20BT–Na50 ~ 90 pC/N). The enhancement in piezoresponse has been attributed to an optimized presence of polar-structural heterogeneity/disorder in the poled ceramic matrix and an optimized distortion of the long-range tetragonal ferroelectric phase. It is established that A-site off-stoichiometry is influencing the polar-structural heterogeneity/disorder and tetragonal lattice distortion via the grain size.

1 Introduction

Ferroelectric and piezoelectric materials are widely used as pressure sensors, actuators, ultrasonic transducers, and multi-layer ceramic capacitors [1–5]. The ferroelectric and piezoelectric materials currently dominating the international market are mostly lead zirconium titanate (PZT) based, owing to their high electromechanical properties [6]. The fundamental science behind the superior performance of PZT-based material is also being keenly studied [7–9]. However, PZT contains more than 40 weight% lead (Pb), which renders it toxic for human health and the environment. Therefore, to

Address correspondence to E-mail: mishraanupam0@gmail.com

https://doi.org/10.1007/s10854-021-05895-6
Published online: 20 April 2021

discourage the use of lead, governing agencies worldwide have imposed strict legislation [10, 11]. This has mandated researchers to look for a suitable lead-free alternatives to PZT, which show similar if not superior properties [12–17].

$Na_{0.5}Bi_{0.5}TiO_3$ (NBT)-based piezoelectric systems are being extensively pursued by research groups across the world since the past two decades. They have shown the potential to replace PZT-based systems owing to their moderate piezoresponse and high electrostrain [18–22]. Their electromechanical properties are also easily reproducible, which make them industrially scalable. The inherent structural complexities present in NBT-based systems make their structure–property correlation studies very intriguing [14, 23]. Among the NBT-based systems, the solid solution of $Na_{0.5}Bi_{0.5}TiO_3$ (NBT) and $BaTiO_3$ (BT), commonly known as NBT–BT has been under focus for the past three decades [24–27]. This solid solution forms the morphotropic phase boundary (MPB) at 6 mol% $BaTiO_3$ (BT) doping in the NBT matrix [24]. The MPB composition is commonly known as NBT–6BT, and it shows a high longitudinal piezoelectric response (d_{33}) of 200 pC/N [28]. It is also interesting from the structural perspective as it shows a high symmetry cubic ($Pm\ \bar{3}m$) structure in X-Ray diffraction studies [28–30]. However, techniques like transmission electron microscopy, nuclear-magneto resonance, and neutron powder diffraction highlight the structural complexities prevalent at the nanoscale in the NBT–6BT matrix [31–36]. Transmission electron microscopy studies have shown the coexistence of rhombohedral ($R3c$) and tetragonal ($P4bm$) phases in NBT–6BT [31, 35, 36]. Groszewicz et al., through ^{23}Na NMR study, reported the coexistence of cubic and polar local symmetries in the MPB composition NBT–6BT [32, 33]. Garg et al. stated that NBT–6BT has a long-period-modulated structure by analyzing neutron powder diffraction data [34]. The structural complexity of NBT–6BT is assumed to be inherited from the parent compound NBT [28, 31, 34]. NBT was considered to be a rhombohedral $R3c$ ferroelectric ever since its discovery by Smolenskii et al. in 1961 [37]. However, recent high-resolution diffraction experiments have indicated that the unpoled structure of NBT belongs to the lower symmetry monoclinic Cc phase [38–40]. Balagurov et al. through neutron diffuse-scattering and Thomas et al. through X-ray diffuse-scattering study have reported that NBT has a long-period-modulated structure [41, 42]. Application of strong electric field (poling) results in the establishment of long-range rhombohedral ($R3c$) ferroelectric order in NBT [39, 40]. The $0.97Na_{0.5}Bi_{0.5}TiO_3$–$0.03BaTiO_3$ (NBT–3BT) composition has also been investigated with utmost interest owing to its inherent structural complexities. Neutron powder diffraction and electron diffraction studies on NBT–3BT report the presence of out of phase $½\{ooo\}_{pc}$ octahedral tilt in the ferroelectric matrix [35, 43]. Badri et al. had reported a premorphotropic phase boundary like characteristic for NBT–3BT [43]. The postmorphotropic phase boundary (MPB) region (beyond 7% BT doping) which is known to have a tetragonal structure has been relatively less studied [25–27, 44]. Badri et al. reported that in the post-MPB regime, the composition of $0.80Na_{0.5}Bi_{0.5}TiO_3$–$0.20BaTiO_3$ (NBT–20BT) shows the highest tetragonality among the compositions of the NBT–BT series [44]. The authors also stated that NBT–20BT has a simple non-modulated tetragonal structure with the absence of oxygen octahedral tilt like the classical ferroelectric $BaTiO_3$. A-site off-stoichiometry technique has been used successfully in case of the structurally complicated systems like parent compound NBT, the premorphotropic phase boundary composition NBT–3BT, and the morphotropic phase boundary composition NBT–6BT, to enhance their piezoresponse substantially. However, no report is present in the literature regarding the effect of off-stoichiometry, on the structurally simpler tetragonal composition NBT–20BT.

In this paper, we have reported the effect of A-site off-stoichiometry on the microstructure, structure, and electromechanical properties of the NBT–20BT composition. The compositions were prepared according to the formulae $0.80Na_{0.5\pm x}Bi_{0.5}TiO_3$–$0.20BaTiO_3$ and $0.80Na_{0.5}Bi_{0.5\pm x}TiO_3$–$0.20BaTiO_3$. For the sake of simplicity, we followed the approach of past studies and varied only one A-site element at a time, i.e., when Na concentration was varied, Bi concentration was kept fixed, and vice versa [45–48]. Ba concentration was kept fixed throughout the study. The compositions are named according to the mole percentage of Na/Bi. For e.g., $0.80Na_{0.48}Bi_{0.5}TiO_3$–$0.20BaTiO_3$ is referred to as 20BT–Na48, $0.80Na_{0.5}Bi_{0.54}TiO_3$–$0.20BaTiO_3$ is referred to as 20BT–Bi54, and the stoichiometric composition $0.80Na_{0.5}Bi_{0.5}TiO_3$–$0.20BaTiO_3$ is referred to as 20BT–Na50/20BT–Bi50 depending on the context of use. After

careful structural investigation, the inherent correlation of the piezoresponse with the polar-structural heterogeneity/disorder prevalent in the poled ceramic matrix and the lattice distortion of the ferroelectric phase is established.

2 Experimental

A-site off-stoichiometric compositions of NBT–20BT were prepared by the traditional solid-state ceramic synthesis method. High-purity powders of Na_2CO_3 (99.9%, Alfa Aesar), Bi_2O_3 (99.9%, SRL), $BaCO_3$ (99.8%, Alfa Aesar), and TiO_2 (99.8%, Alfa Aesar) were dried in a hot air oven at 200 °C for 24 h to remove the absorbed moisture. The dried powders were weighed according to their nominal formulae $0.80Na_{0.5\pm x}Bi_{0.5}TiO_3$–$0.20BaTiO_3$ and $0.80Na_{0.5}Bi_{0.5\pm x}TiO_3$–$0.20BaTiO_3$ (x = 0, 0.02, 0.04, and 0.06). The powders were stirred in yttria-stabilized zirconia vials having yttria-stabilized zirconia balls using a planetary ball mill (Fritsch, P5, Germany) at 200 rpm for 8 h. Acetone was used as the mixing media for better homogenization. The ball-milled powders were calcined at 900 °C for 3 h in a muffle furnace (Delta power, India). The calcined powders were again re-ball milled followed by recalcination to ensure complete perovskite phase formation. Polyvinyl Alcohol (PVA) binder was added to the recalcined powders. The powders were pelletized at 100 MPa. The green pellets obtained were iso-statically pressed at 300 MPa in an incompressible oil medium using a customized die for uniform and enhanced densification. The iso-statically pressed pellets were sintered at 1200 °C for 3 h inside the MgO-sealed alumina cup cone arrangement with spacer powder to minimize Na and Bi′s loss. The density of the sintered pellets was measured using the Archimedes liquid displacement method. The sintered pellets of all the compositions were found to be more than 95% dense. The sintered pellets were mirror polished and thermally etched at 1150 °C for 15 min. Thermally etched pellets were gold sputtered to avoid charging during scanning electron microscopy (SEM) imaging. Scanning electron micrographs (FESEM, Zeiss) of the gold-coated thermally etched pellets were captured at an accelerating voltage of 5 kV and a working distance of 10 mm in the secondary electron mode. The grain size distribution was analyzed by the linear intercept method with the aid of the ImageJ software [49, 50]. Around 350 grains from different regions of the specimen were considered for reliable statistical information. The pellets were thinned down to 0.5 mm thickness and were electroded with silver paste on both sides for electrical characterization. The thinning down of pellets increases their dielectric breakdown strength [51]. The room-temperature resistivity of the silver-painted pellets was measured using an electrometer (Keithley, 6514). The silver-electroded pellets were poled in an insulating silicone oil medium at a dc electric field of 120 kV/cm for 1 h using a high voltage dc power source (IATOME, India). The longitudinal piezoelectric response (d_{33}) of the poled pellets was measured using a Berlincourt meter by applying a force of 0.25 N at a frequency of 110 Hz (Piezotest, PM300, UK). After this, the poled pellets were crushed to powder. The powder, thus, obtained is termed as "poled powder." "Poled powder" was then annealed at 700 °C for 1 h to remove the poling related memory, and the resultant powder obtained is termed as "unpoled powder." The ferroelectric and piezoelectric loops were measured on silver-pasted pellets at an electric field of 70 kV/cm with a frequency of 1 Hz at room temperature in a silicone oil bath using a ferroelectric workstation (Radiant technologies Inc, USA) enabled with a laser interferometer (MTI 2100, USA). X-ray powder diffraction (XRPD) measurement was carried out on the unpoled and poled powders in the 2θ range of 15°–120° at a scan rate of 1°/min with a step size of 0.01° using a high-resolution laboratory X-ray diffractometer (Smartlab, Rigaku, Japan) operating at 4.5 kW power with a rotating copper anode enabled with a Germanium single crystal monochromator in the source arm. Room-temperature dielectric measurements were carried out on unpoled and poled pellets in the frequency range of 10–10^6 Hz with an ac signal of 1 V amplitude using an impedance analyzer (Novocontrol, Montabeur, Germany). Structural analysis of the X-Ray diffraction data was carried out by the Rietveld refinement technique using the FullProf software package [52].

3 Results

3.1 Microstructural characterization

The scanning electron micrographs of the Na-varying and Bi-varying compositions of the NBT–20BT series are shown in Fig. 1. A compact, homogeneous, and pore-free microstructure with clear grain boundaries

is observed for both Na-varying and Bi-varying compositions of the NBT–20BT series. This agrees with a density of 95% obtained for the sintered pellets via the Archimedes liquid displacement method. The Na-varying compositions 20BT–Na44, 20BT–Na46, 20BT–Na48, 20BT–Na50, 20BT–Na52, and 20BT–Na54 have grain sizes of 1.7 μm, 1.9 μm, 2.0 μm, 2.3 μm, 4.9 μm, and 5.9 μm, respectively. The Bi-varying composition 20BT–Bi46, 20BT–Bi48, 20BT–Bi50, 20BT–Bi52, and 20BT–Bi54 have grain sizes of 2.1 μm, 2.2 μm, 2.3 μm, 1.9 μm, and 1.4 μm, respectively. For the Na-varying compositions, the grain size is directly related to the Na concentration in the NBT–20BT matrix. Lower Na concentration leads to a smaller grain size with 20BT–Na44 (1.7 μm) showing the minimum grain size, and higher Na concentration leads to a larger grain size with 20BT–Na54 (5.9 μm) showing the maximum grain size among the Na-varying compositions. In the case of Bi-varying compositions, both Bi excess and Bi deficiency lead to a decrease in grain size, with the stoichiometric composition 20BT–Bi50 (2.3 μm) having the maximum grain size. Recently reported off-stoichiometric studies on NBT-based compositions have shown similar trends [45, 46].

3.2 Room-temperature resistivity

Piezoelectric and ferroelectric materials are technologically useful if they have an insulating/resistive character [53, 54]. Therefore, we measured the resistivity of the Na-varying and Bi-varying specimens of NBT–20BT at room temperature. The room-temperature resistivity of the Na-varying and Bi-varying compositions of the NBT–20BT series is plotted in Fig. 2 as a function of Na/Bi off-stoichiometry. The Na-varying compositions 20BT–Na44, 20BT–Na46, 20BT–Na48, 20BT–Na50, 20BT–Na52, and 20BT–Na54 have resistivity of 0.86×10^9 Ωcm, 0.87×10^9 Ωcm, 0.86×10^9 Ωcm, 0.69×10^9 Ωcm, 0.51×10^9 Ωcm, and 0.05×10^9 Ωcm, respectively. The Bi-varying composition 20BT–Bi46, 20BT–Bi48, 20BT–Bi50, 20BT–Bi52, and 20BT–Bi54 have resistivity of 0.59×10^9 Ωcm, 0.64×10^9 Ωcm, 0.69×10^9 Ωcm, 0.87×10^9 Ωcm, and 0.88×10^9 Ωcm, respectively.

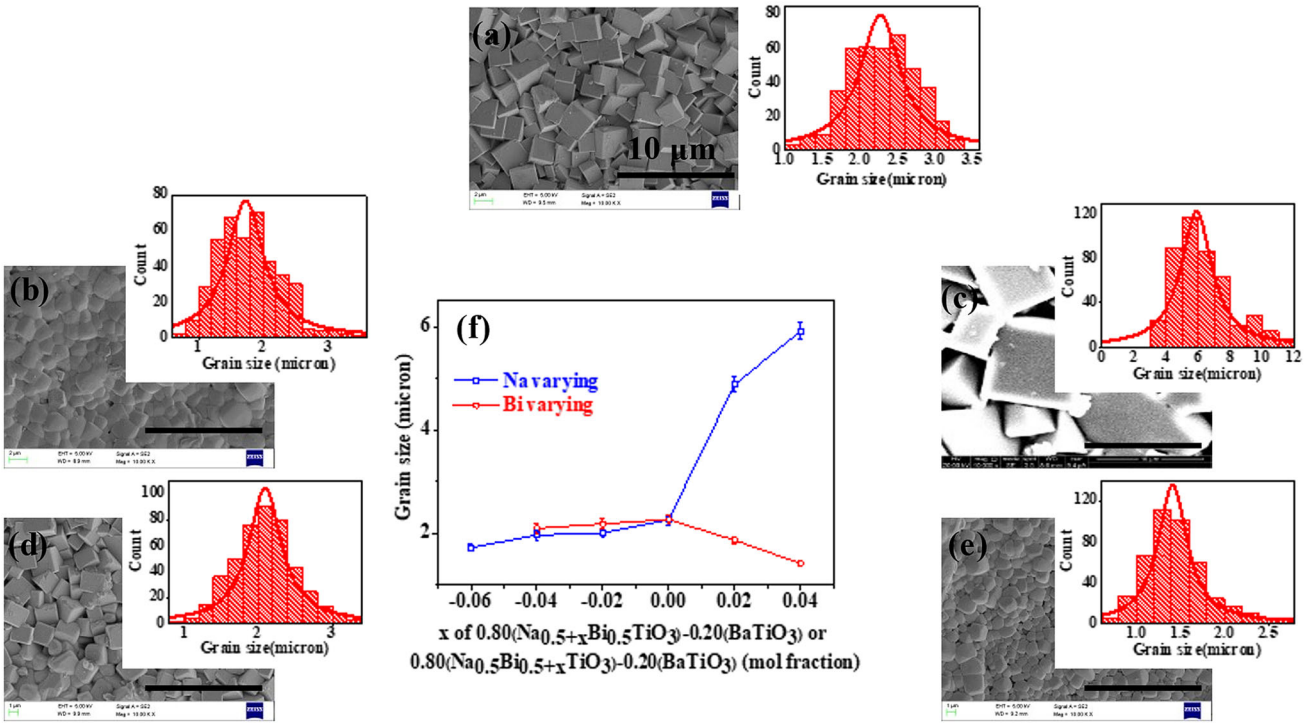

Fig. 1 Scanning electron micrographs and grain size distribution plots of (**a**) $Na_{0.5}Bi_{0.5}TiO_3$–$20BaTiO_3$ (20BT–Na50), (**b**) $Na_{0.44}Bi_{0.5}TiO_3$–$20BaTiO_3$ (20BT–Na44), (**c**) $Na_{0.54}Bi_{0.5}TiO_3$–$20BaTiO_3$ (20BT–Na54), (**d**) $Na_{0.5}Bi_{0.46}TiO_3$–$20BaTiO_3$ (20BT–Bi46), (**e**) $Na_{0.5}Bi_{0.54}TiO_3$–$20BaTiO_3$ (20BT–Bi54). The scale bar shown in the right-hand bottom corner of the SEM images corresponds to 10 μm length. (**f**) The variation of the average grain size as a function of off-stoichiometry for both the Na-varying and Bi-varying compositions of the NBT–20BT series. The error bars are shown along with the data points

For the Na–series specimens, the specimens' resistivity decreases with Na concentration with 20BT–Na46 (0.87×10^9 Ωcm) showing the maximum resistivity and 20BT–Na54 (0.05×10^9 Ωcm) showing the minimum resistivity. In case of the Bi-series specimens, the samples' resistivity increases with Bi concentration with 20BT–Bi46 (0.59×10^9 Ωcm) showing the minimum resistivity and 20BT–Bi54 (0.88×10^9 Ωcm) showing the maximum resistivity. Na deficiency/Bi excess makes the NBT–20BT matrix more insulating. This is in tune with previous reports [45, 46, 55–57].

3.3 Ferroelectric and piezoelectric behavior

The ferroelectric (polarization(P)-electric field(E)) and piezoelectric (strain(S)-electric field(E)) hysteresis loops corresponding to the Na-varying and Bi-varying compositions of the NBT–20BT series are shown in Fig. 3. It was impossible to obtain saturated ferroelectric loops for Na-excess and Bi-deficient specimens due to their lower resistivity/higher conductivity. It is observed that a minimum resistivity of 0.69×10^9 Ωcm is required to obtain non-lossy and well-saturated ferroelectric hysteresis loop. The Na-deficient and Bi-excess compositions of the NBT–20BT series yield well-saturated ferroelectric and piezoelectric hysteresis loops at an ac electric field amplitude of 70 kV/cm and a frequency of 1 Hz. 20BT–Na44, 20BT–Na46, 20BT–Na48, and

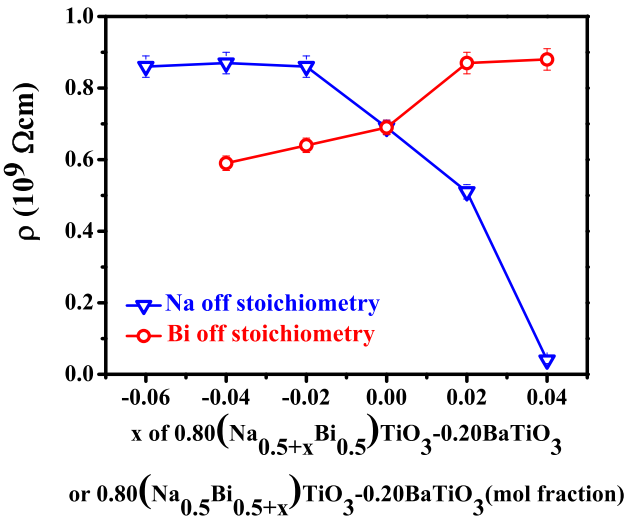

Fig. 2 Variation of room-temperature resistivity with off-stoichiometry for both the Na- and Bi-varying compositions of the NBT–20BT series. The error bars are shown along with the data points

20BT–Na50 have remnant polarization (P_r) of 31 μC/cm^2, 45 μC/cm^2, 39 μC/cm^2, and 38 μC/cm^2, respectively. 20BT–Bi50, 20BT–Bi52, and 20BT–Bi54 have remnant polarization (P_r) of 38 μC/cm^2, 39 μC/cm^2, and 38 μC/cm^2, respectively (Fig. 4a). The coercive field (E_c) of 20BT–Na44, 20BT–Na46, 20BTNa48, and 20BT–Na50 are 32 kV/cm, 38 kV/cm, 44 kV/cm, and 43 kV/cm, respectively. 20BT–Bi50, 20BT–Bi52, and 20BT–Bi54 have coercive field (E_c) of 43 kV/cm, 29 kV/cm, and 39 kV/cm, respectively (Fig. 4b). The maximum electrostrain (S_{max}) obtained for 20BT–Na44, 20BT–Na46, 20BTNa48, and 20BT–Na50, are 0.12%, 0.14%, 0.12%, and 0.11%, respectively. The maximum electrostrain obtained for 20BT–Bi50, 20BT–Bi52, and 20BT–Bi54, are 0.11%, 0.16%, and 0.14%, respectively (Fig. 4c). The maximum electrostrain (S_{max}) was also measured as a function of the electric field. The maximum electrostrain (S_{max}) of the stoichiometric composition 20BT–Na50 and the off-stoichiometric compositions 20BT–Na46 and 20BT–Bi52 is plotted as a function of electric field in Fig. 4d. The stoichiometric composition 20BT–Na50 shows an electrostrain of 0.07%, 0.09%, 0.10%, and 0.11% at a field 40 kV/cm, 50 kV/cm, 60 kV/cm, and 70 kV/cm, respectively. The composition 20BT–Na46 shows an electrostrain of 0.09%, 0.11%, 0.13%, and 0.14% at a field of 40 kV/cm, 50 kV/cm, 60 kV/cm and 70 kV/cm, respectively. The composition 20BT–Bi52 shows an electrostrain of 0.10%, 0.12%, 0.15%, and 0.16% at a field of 40 kV/cm, 50 kV/cm, 60 kV/cm and 70 kV/cm, respectively. The maximum electrostrain (S_{max}) shows a linear increase with field amplitude for all the compositions. From the above reported ferroelectric (P_r and E_c) and piezoelectric (S_{max}) parameters, it is evident that an optimized Na deficiency and Bi excess in the NBT–20BT matrix helps in reducing the coercive field (E_c) and enhancing the remnant polarization (P_r) and electrostrain (S_{max}). The enhancement in remnant polarization, electrostrain, and decrease in the coercive field indicates the greater ease of domain switching in Na-deficient/Bi-excess compositions [47, 48].

The longitudinal piezoelectric response (d_{33}) of the Na-varying and Bi-varying NBT–20BT compositions are shown in Fig. 5. The Na-varying compositions 20BT–Na44, 20BT–Na46, 20BT–Na48, 20BT–Na50, 20BT–Na52, and NaBT–Na54, have d_{33} of 83 pC/N, 115 pC/N, 99 pC/N, 91 pC/N, 62 pC/N, and 56 pC/N, respectively. The Bi-varying composition 20BT–

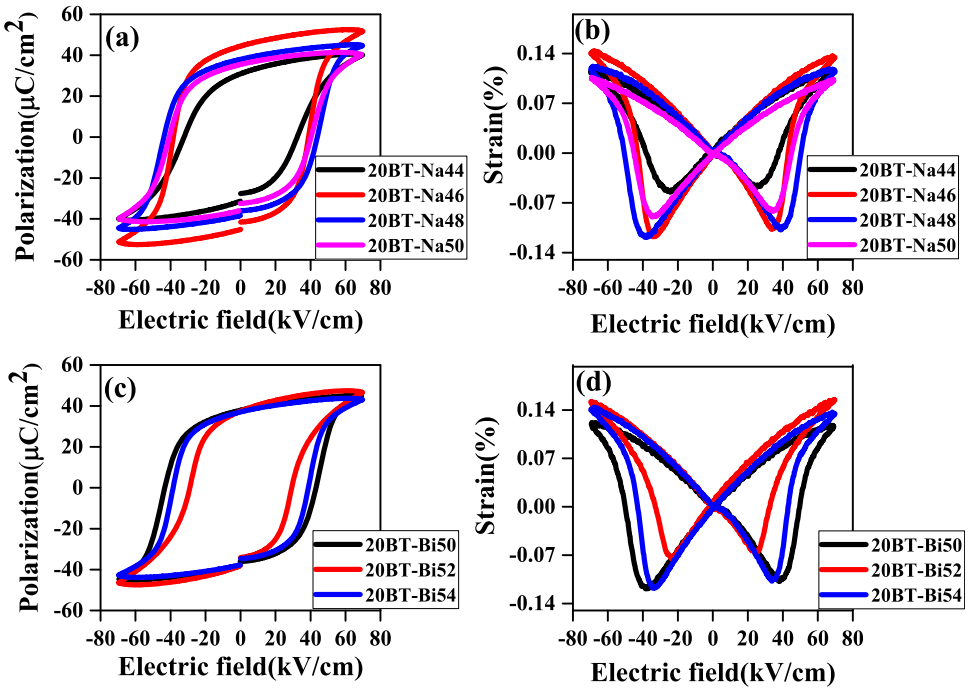

Fig. 3 (**a**) and (**b**) The polarization (P)-electric field (E) (ferroelectric) and strain (S)-electric field (E) (piezoelectric) hysteresis loops for the Na-varying compositions of the NBT–20BT series. (**c**) and (**d**) The polarization (P)-electric field (E) (ferroelectric) and strain (S)-electric field (E) (piezoelectric) hysteresis loops for the Bi-varying compositions of the NBT–20BT series. The hysteresis loops were measured at room temperature with an ac field amplitude of 70 kV/cm and 1 Hz frequency

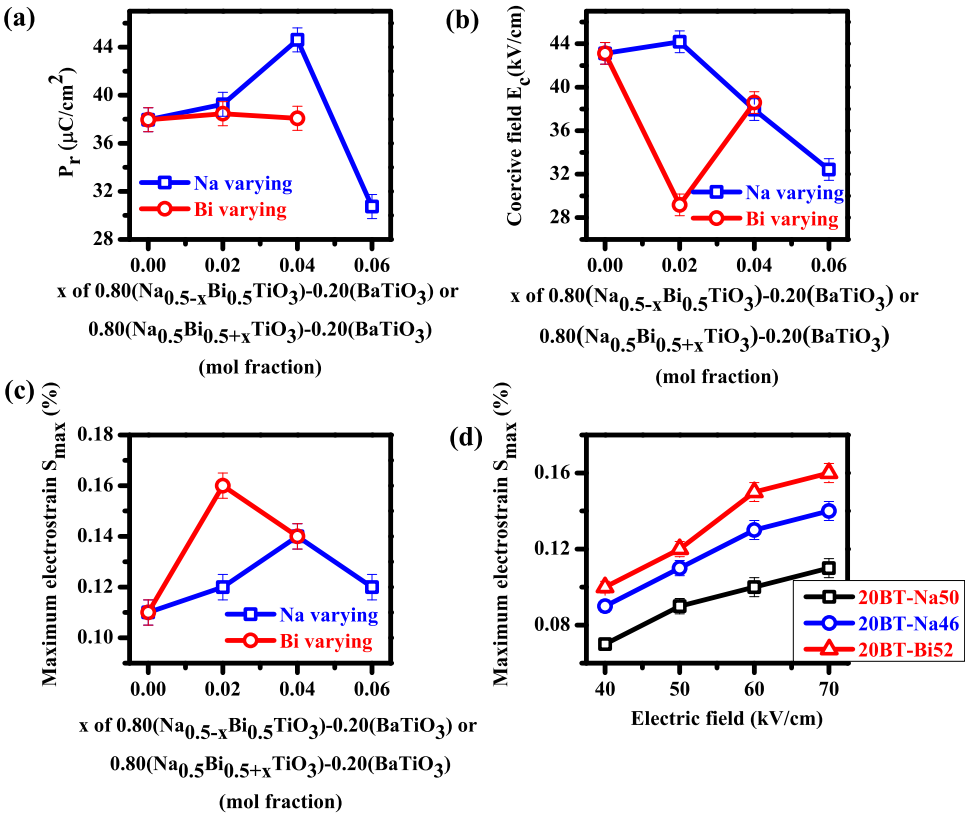

Fig. 4 (**a**) Remanent polarization (P_r), (**b**) coercive field (E_c), (**c**) maximum electrostrain (S_{max}) for the Na-varying and Bi-varying compositions of NBT–20BT series and (**d**) maximum electrostrain as a function of electric field for 20BT–Na50, 20BT–Na46, and 20BT–Bi52. The remnant polarization (P_r) and coercive field (E_c) were obtained from the ferroelectric hysteresis loop. The maximum electrostrain (S_{max}) was obtained from the piezoelectric hysteresis loop. The ferroelectric and piezoelectric hysteresis loop were measured at room temperature with an ac field amplitude of 70 kV/cm and 1 Hz frequency. The error bars are shown along with the data points

Bi46, 20BT–Bi48, 20BT–Bi50, 20BT–Bi52, and 20BT–Bi54, have d_{33} of 37 pC/N, 49 pC/N, 91 pC/N, 114 pC/N, and 102 pC/N, respectively. While the maximum piezoelectric response obtained in the Na-varying series is in the Na-deficient regime (20BT–Na46 ~ 115 pC/N), in case of the Bi-varying series, the maximum piezoresponse is obtained in the Bi-excess regime (20BT–Bi52 ~ 114 pC/N). However,

when the Na deficiency is increased beyond a certain limit from 20BT–Na46 to 20BT–Na44, the piezoresponse decreases from 115 to 83 pC/N. Similarly, when the Bi excess is increased from 20BT–Bi52 to 20BT–Bi54, the piezoresponse decreases from 114 to 102 pC/N. The enhancement in piezoresponse in the Na-deficient and Bi-excess regime is related to the increased ease of domain switching [47, 48].

3.4 Global structure study by X-ray powder diffraction (XRPD)

$\{110\}_{pc}$, $\{111\}_{pc}$, $\{200\}_{pc}$, and $\{211\}_{pc}$ Bragg profiles of unpoled and poled Na-varying specimens are shown in Fig. 6. The poled compositions of the Na-varying specimens of the NBT–20BT compositions have a clear tetragonal distortion, which is indicated by the doublet nature of $\{110\}_{pc}$,$\{200\}_{pc}$, and $\{211\}_{pc}$ Bragg profiles and singlet nature of the $\{111\}_{pc}$ Bragg profile. The unpoled composition in the Na-deficient regime 20BT–Na44, 20BT–Na46, and 20BT–Na48 show a strong intermediate peak corresponding to the cubic phase (marked for unpoled and poled 20BT–Na44) in the $\{110\}_{pc}$, $\{200\}_{pc}$, and $\{211\}_{pc}$ Bragg profiles. The application of electric field (poling) suppresses the cubic phase and strengthens the long-range ferroelectric tetragonal phase.

$\{110\}_{pc}$, $\{111\}_{pc}$, $\{200\}_{pc}$, and $\{211\}_{pc}$ Bragg profiles of unpoled and poled Bi-varying specimens are shown in Fig. 7. Like the Na-varying compositions, the poled Bi-varying compositions show a long-range tetragonal order. The unpoled composition in the Bi-excess regime 20BT–Bi52 and 20BT–Bi54 shows a strong intermediate peak corresponding to the cubic phase in the $\{110\}_{pc}$, $\{200\}_{pc}$, and $\{211\}_{pc}$ Bragg profiles (marked for unpoled and poled 20BT–Bi54). Like the Na-varying compositions, the cubic phase is suppressed after application of the electric field, and a long-range tetragonal distortion is stabilized

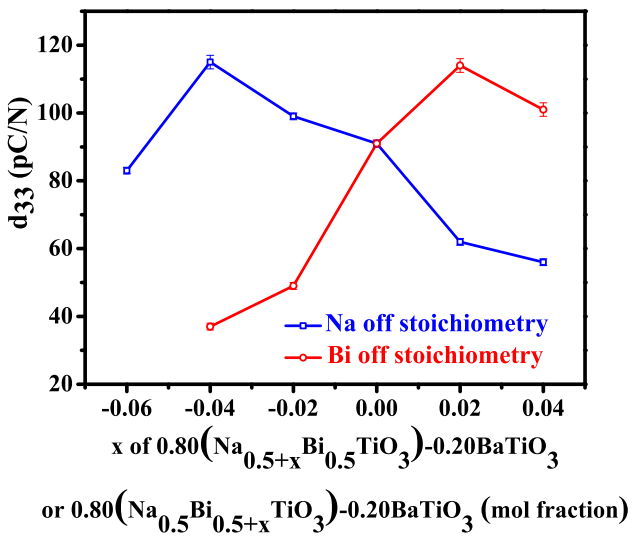

Fig. 5 Variation of longitudinal piezoelectric coefficient (d_{33}) with off-stoichiometry for both Na- and Bi-varying compositions of the NBT–20BT series. The error bars are shown along with the data points

Some recent studies have correlated piezoresponse with the cubic phase fraction present in the ferroelectric matrix. They have shown that the piezoresponse maximizes at an optimized cubic phase fraction [45, 46]. To establish the correlation in NBT–20BT, the poled compositions of 20BT–Na44, 20BT–Na46, 20BT–Na48, and 20BT–Na50 were fitted with the $Pm\,\bar{3}m + P4mm$ (cubic + tetragonal) dual-phase coexistence model (Fig. 8). The refined structural parameters are given in Tables 1, 2, 3, and 4. While the tetragonal phase corresponds to the long-range ferroelectric distortion, the cubic phase quantifies the polar-structural heterogeneity/disorder prevalent in the ferroelectric matrix [58–62]. The cubic phase fraction obtained for poled 20BT–Na44, 20BT–Na46, 20BT–Na48, and 20BT–Na50 are 32%, 25%, 20%, and 15% respectively. It is observed that the composition 20BT–Na46 showing the highest piezoresponse (115 pC/N) has an optimized cubic phase fraction of 25% (Fig. 9a). When the cubic phase fraction increases to 32% for 20BT–Na44, the piezoresponse decreases to 83 pC/N. The tetragonality/lattice distortion in percentage was calculated by using the formula $((\frac{c}{a} - 1)*100)$ where c and a are the lattice parameters of the $P4mm$ phase. The tetragonality for poled 20BT–Na44, 20BT–Na46, 20BT–Na48, and 20BT–Na50 was found to be 1.8%, 1.9%, 2.0%, and 2.1%. The maximum piezoresponse of 115 pC/N was obtained for 20BT–Na46, which had a tetragonality of 1.9% (Fig. 9b). When the tetragonality decreases to 1.8% for 20BT–Na44, the piezoresponse reduced to 83 pC/N. This indicates that the piezoresponse maximizes at an optimized cubic phase fraction (disorder) and long-range tetragonal lattice distortion in the poled ferroelectric matrix.

3.5 Dielectric dispersion behavior

The dielectric dispersion (permittivity vs ln frequency) plots for the unpoled and poled specimens

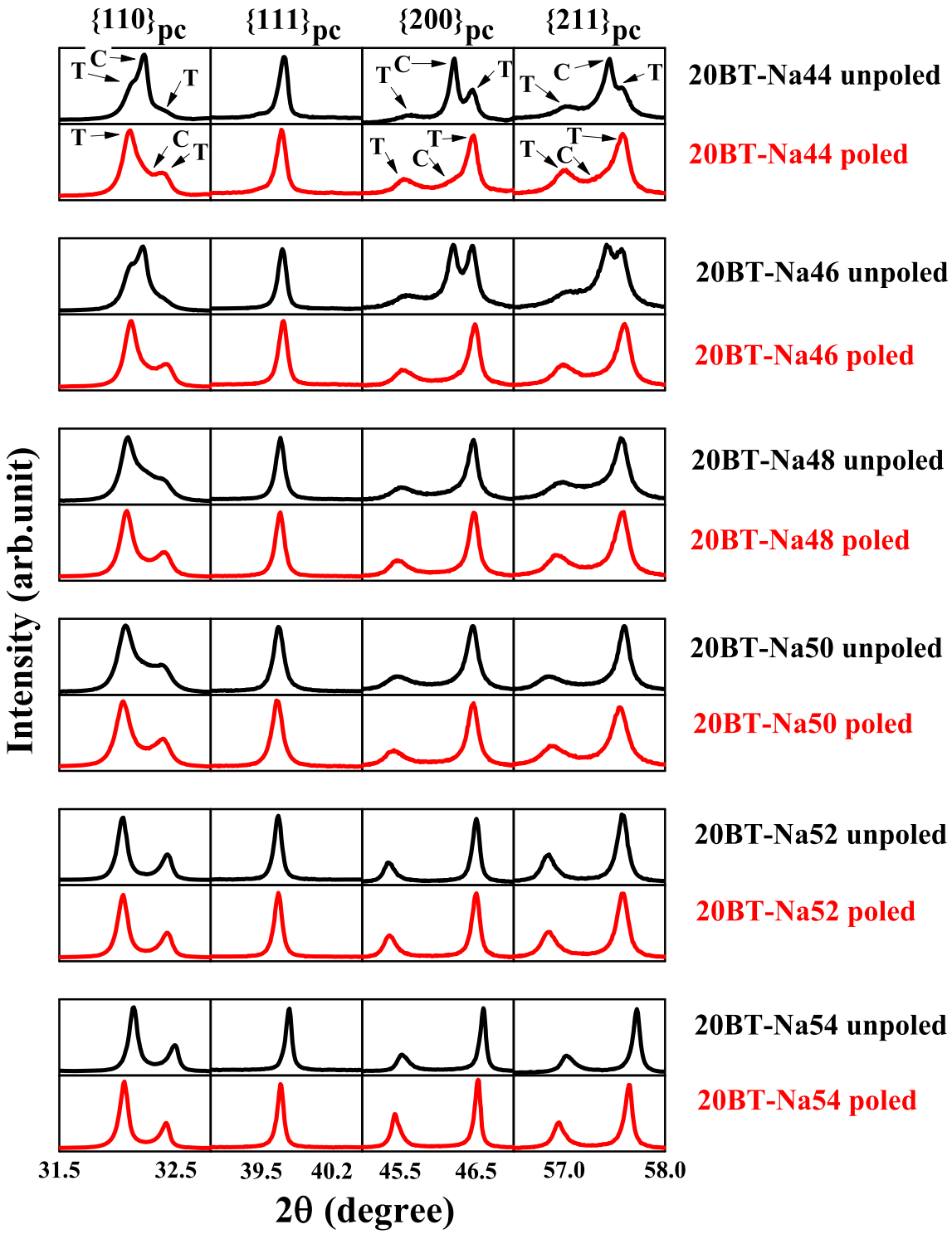

Fig. 6 Selected XRPD pseudo-cubic Bragg profiles of unpoled (black) and poled (red) Na-varying compositions of NBT–20BT series. The peaks corresponding to tetragonal and cubic phases are highlighted for the composition 20BT–Na44 for better comprehension (Color figure online)

of the stoichiometric and Na-deficient compositions of the NBT–20BT series are shown in Fig. 10. The slope of the dielectric dispersion plots can be considered to be a quantitative measure of the polar-structural heterogeneity/disorder in the ferroelectric matrix as a function of some tuning parameter

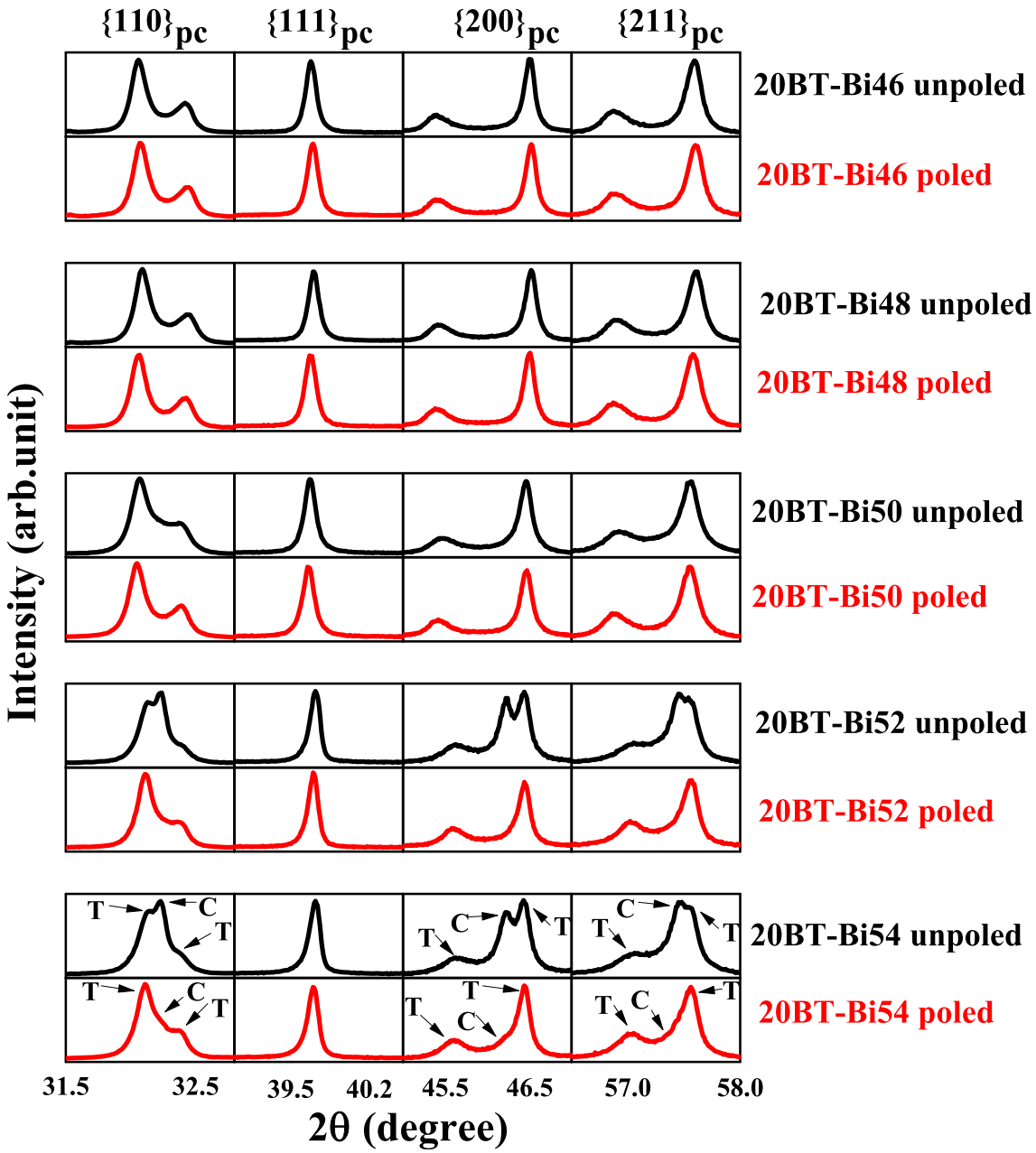

Fig. 7 Selected XRPD pseudo-cubic Bragg profiles of unpoled (black) and poled (red) Bi-varying compositions of NBT–20BT series. The peaks corresponding to tetragonal and cubic phases are highlighted for the composition 20BT–Bi54 for better comprehension (Color figure online)

[34, 45, 46, 63–65]. Here the tuning parameter is the variation of Na concentration in the NBT–20BT matrix. Unpoled 20BT–Na44, 20BT–Na46, 20BT–Na48 (not shown), and 20BT–Na50 have slopes of − 52.1, − 25.8, − 22.3, and − 17.9 respectively. On application of electric field (poling) the slope reduces to − 43.7, − 8.1, − 7.1, and − 4.2 for 20BT–Na44, 20BT–Na46, 20BT–Na48 (not shown), and 20BT–Na50, respectively. Application of electric field establishes long-range ferroelectric order by "wiping out" local positional disorder [66–68]. "Degree of ordering" (Δ*s*) has been defined as a measure of the effectiveness of the electric field in establishing long-range order in the ferroelectric matrix [45, 46, 65]. It is calculated for a given composition by subtracting the unpoled slope from the poled slope. The degree of ordering (Δ*s*) for

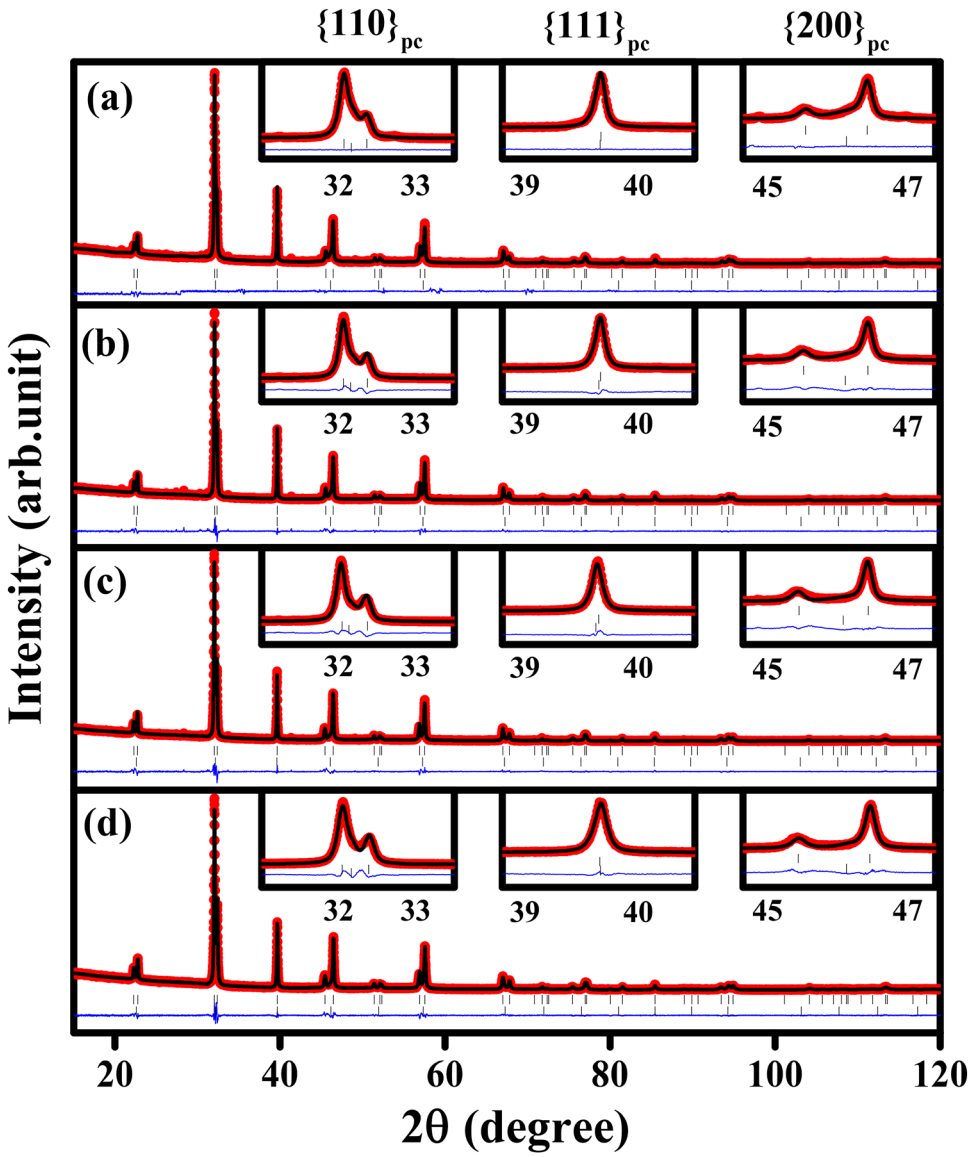

Fig. 8 Rietveld fitted XRPD patterns of poled (**a**) 20BT–Na44, (**b**) 20BT–Na46, (**c**) 20BT–Na48, and (**d**) 20BT–Na50 compositions of the NBT–20BT series with cubic + tetragonal ($Pm\bar{3}m + P4mm$) phase coexistence model

20BT–Na44, 20BT–N46, 20BT–Na48, and 20BT–Na50 are 8.4, 17.7, 15.2, and 13.7, respectively. It is observed that the composition 20BT–Na46 showing the maximum degree of ordering (17.7) has the highest piezoresponse of 115 pC/N. This indicates that irrespective of the initial polar-structural heterogeneity/disorder present in the ferroelectric matrix, the applied electric field's effectiveness in overcoming the local structural/positional inhomogeneity, and establishing a long-range ferroelectric order will determine the piezoresponse [45, 46].

4 Discussion

The inherent polar-structural heterogeneity and their influence on the electromechanical properties make NBT-based system very scientifically intriguing [14, 28]. Various techniques ranging from cationic off-stoichiometry to "grain size" engineering have been utilized successfully to enhance these systems' electromechanical properties by indirectly controlling the polar-structural heterogeneity present in the ferroelectric matrix [45, 47, 48, 69, 70]. A-site cationic off-stoichiometry has been used to improve the piezoresponse for NBT, the premorphotropic phase boundary composition NBT–3BT and the morphotropic phase boundary composition NBT–6BT

Table 1 Refined structural parameters of X-Ray powder diffraction (XRPD) data of poled 20BT–Na44 with cubic ($Pm\bar{3}m$) + tetragonal ($P4mm$) dual-phase structural model

Atomic coordinates	x	y	z	Isotropic thermal parameters (Å^2)
Cubic ($Pm\bar{3}m$) structural parameters of poled 20BT–Na44				
Na/Bi/Ba	0	0	0	2.15(7)
Ti	0.5	0.5	0.5	1.98(2)
O	0.5	0.5	0	1.0
Tetragonal ($P4mm$) structural parameters of poled 20BT–Na44				
Na/Bi/Ba	0	0	0	
Ti	0.5	0.5	0.535(2)	
O1	0.5	0.5	− 0.092(5)	1.0
O2	0.5	0	0.408(7)	1.0

Anisotropic thermal parameters for tetragonal phase	U^{11}	U^{22}	U^{33}	U^{12}	U^{13}	U^{23}
Na/Bi/Ba	0.034(2)	0.034(2)	0.054(1)	0	0	0
Ti	0.001(7)	0.001(7)	0.052(9)	0	0	0

Cubic lattice parameters $a = b = c = 3.9325(1)$ Å; Cubic Phase fraction = 32%

Tetragonal lattice parameters $a = 3.9085(1)$ Å; $c = 3.9800(8)$ Å; Tetragonal Phase fraction = 68%

$R_p = 2.36$; $R_{wp} = 3.51$; $R_{exp} = 1.68$; $\chi^2 = 2.18$

Table 2 Refined structural parameters of X-Ray powder diffraction (XRPD) data of poled 20BT–Na46 with cubic ($Pm\bar{3}m$) + tetragonal ($P4mm$) dual-phase structural model

Atomic coordinates	x	y	z	Isotropic thermal parameters (Å^2)
Cubic ($Pm\bar{3}m$) structural parameters of poled 20BT–Na46				
Na/Bi/Ba	0	0	0	2.07(9)
Ti	0.5	0.5	0.5	1.83(1)
O	0.5	0.5	0	1.0
Tetragonal ($P4mm$) structural parameters of poled 20BT–Na46				
Na/Bi/Ba	0	0	0	
Ti	0.5	0.5	0.535(6)	
O1	0.5	0.5	− 0.092(3)	1.0
O2	0.5	0	0.408(2)	1.0

Anisotropic thermal parameters for tetragonal phase	U^{11}	U^{22}	U^{33}	U^{12}	U^{13}	U^{23}
Na/Bi/Ba	0.042(9)	0.042(8)	0.047(5)	0	0	0
Ti	0.001(4)	0.001(1)	0.059(8)	0	0	0

Cubic lattice parameters $a = b = c = 3.9336(4)$ Å; Cubic Phase fraction = 25%

Tetragonal lattice parameters $a = 3.9077(4)$ Å; $c = 3.9825(1)$ Å; Tetragonal Phase fraction = 75%

$R_p = 2.77$; $R_{wp} = 3.62$; $R_{exp} = 1.79$; $\chi^2 = 2.06$

[45–48]. However, the exact mechanism by which off-stoichiometry enhances the piezoresponse remains a topic of contemporary debate. Spreitzer et al. had reported enhancement in the piezoresponse of NBT with Na deficiency [71]. The authors had attributed the enhancement of piezoresponse to the presence of A-site vacancies, which makes domain mobility easier. If A-site vacancies were indeed playing a role in enhancing the piezoresponse, then Bi-deficient NBT, NBT–3BT, and NBT–20BT should show higher piezoresponse than the stoichiometric composition. However, it is observed that Bi-excess compositions show a higher piezoresponse in contrast to the stoichiometric composition [45–47]. This negates the hypothesis proposed by Spreitzer et al. [71]. Sung et al. had attributed the enhancement in piezoresponse in Na-deficient and Bi-excess NBT to the decrease in lattice distortion of the long-ranged ferroelectric phase, which results in the lowering of lattice strain and makes domain switching easier [47, 48]. Mishra et al. attributed the enhancement in piezoresponse with off-stoichiometry for NBT, NBT–3BT, and the morphotropic phase boundary composition NBT–6BT to the optimization of polar-structural heterogeneity/disorder (quantified by the cubic phase) and grain size [45, 46]. In case of NBT–20BT, the composition 20BT–Na46 shows a piezoresponse of 115 pC/N which is more than 25% higher than the piezoresponse of 91 pC/N shown by the stoichiometric composition. Similarly, the composition 20BT–Bi52 shows a piezoresponse of 114 pC/N, which is also a significant enhancement of 25% compared to the stoichiometric composition. The polar-structural heterogeneity (cubic phase) present in the poled specimen of 20BT–Na46 is 25%, while the polar-structural heterogeneity present in the poled stoichiometric composition 20BT–Na50 is 15%. The tetragonal lattice distortion for poled 20BT–Na46 is 1.9%, while 20BT–Na50 has a higher tetragonal lattice distortion of 2.1%. The higher polar-structural

Table 3 Refined structural parameters of X-ray powder diffraction (XRPD) data of poled 20BT–Na48 with cubic ($Pm\bar{3}m$) + tetragonal ($P4mm$) dual-phase structural model

Atomic coordinates	x	y	z	Isotropic thermal parameters (Å^2)
Cubic ($Pm\bar{3}m$) structural parameters of poled 20BT–Na48				
Na/Bi/Ba	0	0	0	2.02(1)
Ti	0.5	0.5	0.5	1.78(5)
O	0.5	0.5	0	1.0
Tetragonal ($P4mm$) structural parameters of poled 20BT–Na48				
Na/Bi/Ba	0	0	0	
Ti	0.5	0.5	0.517(9)	
O1	0.5	0.5	− 0.092(4)	1.0
O2	0.5	0	0.408(1)	1.0

Anisotropic thermal parameters for tetragonal phase	U^{11}	U^{22}	U^{33}	U^{12}	U^{13}	U^{23}
Na/Bi/Ba	0.036(5)	0.036(5)	0.054(8)	0	0	0
Ti	0.003(2)	0.003(2)	0.068(5)	0	0	0

Cubic lattice parameters $a = b = c = 3.9361(7)$ Å; Cubic Phase fraction = 20%

Tetragonal lattice parameters $a = 3.9074(5)$ Å; $c = 3.9879(2)$ Å; Tetragonal Phase fraction = 80%

$R_p = 2.32$; $R_{wp} = 3.21$; $R_{exp} = 1.67$; $\chi^2 = 1.86$

Table 4 Refined structural parameters of X-Ray powder diffraction (XRPD) data of poled 20BT–Na50 with cubic ($Pm\bar{3}m$) + tetragonal ($P4mm$) dual-phase structural model

Atomic coordinates	x	y	z	Isotropic thermal parameters (Å^2)
Cubic ($Pm\bar{3}m$) structural parameters of poled 20BT–Na50				
Na/Bi/Ba	0	0	0	1.95(7)
Ti	0.5	0.5	0.5	1.58(2)
O	0.5	0.5	0	1.0
Tetragonal ($P4mm$) structural parameters of poled 20BT–Na50				
Na/Bi/Ba	0	0	0	
Ti	0.5	0.5	0.518(8)	
O1	0.5	0.5	− 0.092(1)	1.0
O2	0.5	0	0.408(5)	1.0

Anisotropic thermal parameters for tetragonal phase	U^{11}	U^{22}	U^{33}	U^{12}	U^{13}	U^{23}
Na/Bi/Ba	0.032(8)	0.032(8)	0.050(2)	0	0	0
Ti	0.007(2)	0.007(2)	0.072(3)	0	0	0

Cubic lattice parameters $a = b = c = 3.9324(8)$ Å; Cubic Phase fraction = 15%

Tetragonal lattice parameters $a = 3.9058(7)$ Å; $c = 3.9889(2)$ Å; Tetragonal Phase fraction = 85%

$R_p = 2.59$; $R_{wp} = 3.36$; $R_{exp} = 1.85$; $\chi^2 = 1.64$

heterogeneity/disorder and lower ferroelectric lattice distortion of 20BT–Na46 in comparison to 20BT–Na50 result in the enhancement of piezoresponse. However, when the polar-structural heterogeneity increases to 32% and the tetragonal lattice distortion decreases to 1.8% for poled 20BT–Na44, the piezoresponse decreases to 83 pC/N. The structural disorder (cubic phase) can be visualized as a "lubricant," which ensures the easy alignment of long-range ferroelectric domains (tetragonal phase) on application of electrical field by decreasing the "interdomain friction." A low tetragonal lattice distortion results in reduced "intradomain friction," enhancing the switchability of the domains on application of the electric field. However, when the volume fraction of ferroelectric domains (tetragonal phase) decreases beyond a certain limit the piezoresponse diminishes even though the "lubricant" (cubic phase) volume increases. The "grain size" effect could be another plausible reason for enhancing piezoresponse in off-stoichiometric specimens. Recent reports on NBT-based systems have linked the enhancement in piezoresponse to grain size [69, 70, 72–77]. 20BT–Na46 and 20BT–Bi52, which have a grain size of 1.9 μm, show a 25% enhanced piezoresponse ($d_{33} \sim 115$ pC/N) in comparison to the stoichiometric composition 20BT–Na50 ($d_{33} \sim 91$ pC/N) having a grain size of 2.3 μm. When the grain size further decreases to 1.7 μm and 1.4 μm for 20BT–Na44 and 20BT–Bi54, the piezoresponse decreases to 102 pC/N and 83 pC/N. This indicates that the piezoresponse maximizes at an optimized grain size. Therefore, off-stoichiometry could be influencing the piezoresponse by modulating the lattice distortion and polar-structural heterogeneity/disorder via the grain size [45–48]. This study establishes the universal potency of A-site off-stoichiometry in enhancing the piezoresponse and electrostrain in NBT-based systems. We have summarized the effect of A-site off-stoichiometry on the electrical resistivity (ρ), piezoresponse (d_{33}), and maximum electrostrain (S_{max}) of NBT–20BT compositions in Table 5 and have also highlighted the

practical utility for these compositions. The most suitable compositions for pressure sensor and actuator applications are 20BT–Na46 and 20BT–Bi52. It would be of immense fundamental and technological interest in studying the effectiveness of A-site cationic off-stoichiometry technique in enhancing the electromechanical properties of high-performance lead-based materials like Sm-doped $Pb(Mg_{1/3}Nb_{2/3})O_3$–$PbTiO_3$ (PMN–PT) and La-doped $BiFeO_3$–$PbTiO_3$ (BF–PT) [78, 79]. The effect of A-site cationic off stoichiometry in influencing the energy storage behaviour of high performance lead free material like MnO_2 doped NBT-BT-BF and NBT-BT-KNN would also be very intriguing [65, 80].

5 Conclusion

The effect of A-site cationic (Na/Bi) off-stoichiometry on the microstructure, structure, and electromechanical properties of $0.80Na_{0.5}Bi_{0.5}TiO_3$–$0.20BaTiO_3$ (NBT–20BT) ceramics were studied. Polycrystalline specimens with chemical formulae $0.80Na_{0.5\pm x}Bi_{0.5}TiO_3$–$0.20BaTiO_3$ and $0.80Na_{0.5}Bi_{0.5\pm x}TiO_3$–$0.20BaTiO_3$ (x = 0, 0.02 and 0.04) were prepared by the conventional solid-state ceramic synthesis route. It is observed that the grain size increases with Na concentration for the Na-varying compositions, with 20BT–Na44 having the minimum grain size of 1.7 μm and 20BT–Na54 having the maximum grain size of 5.9 μm. For Bi-varying compositions, grain size decreases on either side of the stoichiometric composition. The stoichiometric composition 20BT–Bi50 has the maximum grain size of 2.3 μm for the Bi-varying series. Room-temperature resistivity decreases with Na concentration for the Na-varying compositions with 20BT–Na46 having the maximum resistivity of 0.87×10^9 Ωcm and 20BT–Na54 showing the minimum resistivity of 0.05×10^9 Ωcm. In the case of Bi-varying compositions, room temperature resistivity increases with Bi concentration. The composition with the minimum Bi concentration 20BT–Bi46 has a resistivity of 0.59×10^9 Ωcm, and the composition with the maximum Bi concentration 20BT–Bi54 has a resistivity of 0.88×10^9 Ωcm. Na deficiency and Bi excess lead to a decrease in the coercive field (E_c) and an increase in the remnant polarization (P_r) and electrostrain (S_{max}). Piezoresponse increases upto a certain Na deficiency for the Na-varying compositions with 20BT–Na46 showing the maximum piezoresponse of 115 pC/N. For the Bi-varying compositions, piezoresponse increases in the Bi-excess regime with 20BT–Bi52 showing a piezoresponse of 114 pC/N. These values are 25% higher than the stoichiometric composition's piezoresponse (20BT–Na50/20BT–Bi50 ~ 91 pC/N). However, when Na deficiency and Bi excess increase beyond the optimized limit, the piezoresponse decreases with 20BT–Na44 having a piezoresponse of 83 pC/N and 20BT–Bi54 having a piezoresponse of 102 pC/N. Na deficiency and Bi excess in the NBT–20BT matrix result in enhancement of the polar-structural heterogeneity/positional disorder (quantified by the cubic phase fraction) along with a decrease in the

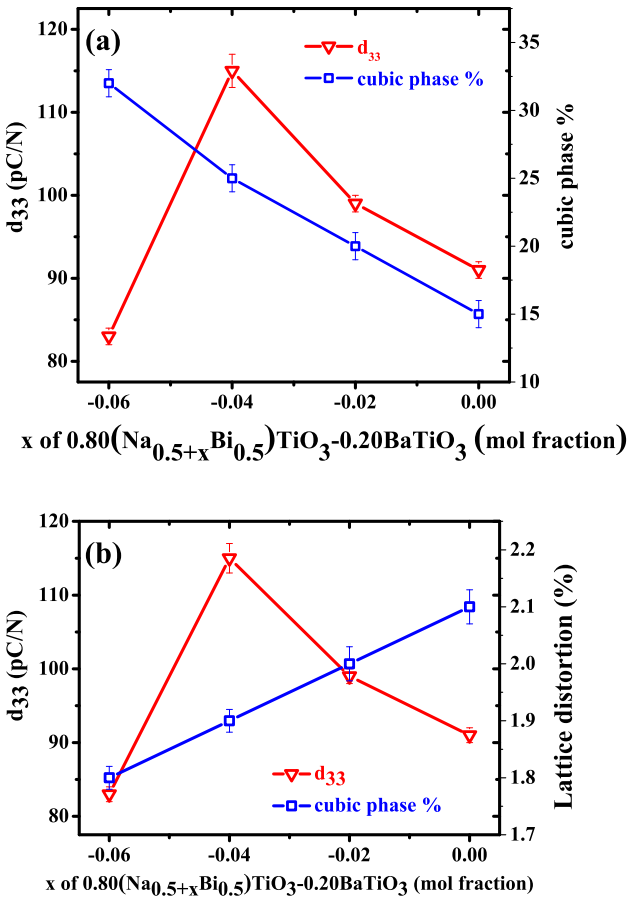

Fig. 9 (**a**) Variation of the longitudinal piezoelectric coefficient (d_{33}) and cubic phase % retained after poling with off-stoichiometry in the Na-deficient region of NBT–20BT series. (**b**) Variation of the longitudinal piezoelectric coefficient (d_{33}) and tetragonal lattice distortion (%) retained after poling with off-stoichiometry in the Na-deficient region of NBT–20BT series. The error bars are shown along with the data points. It is observed that the piezoresponse (d_{33}) maximizes at an optimized cubic phase fraction and tetragonal lattice distortion

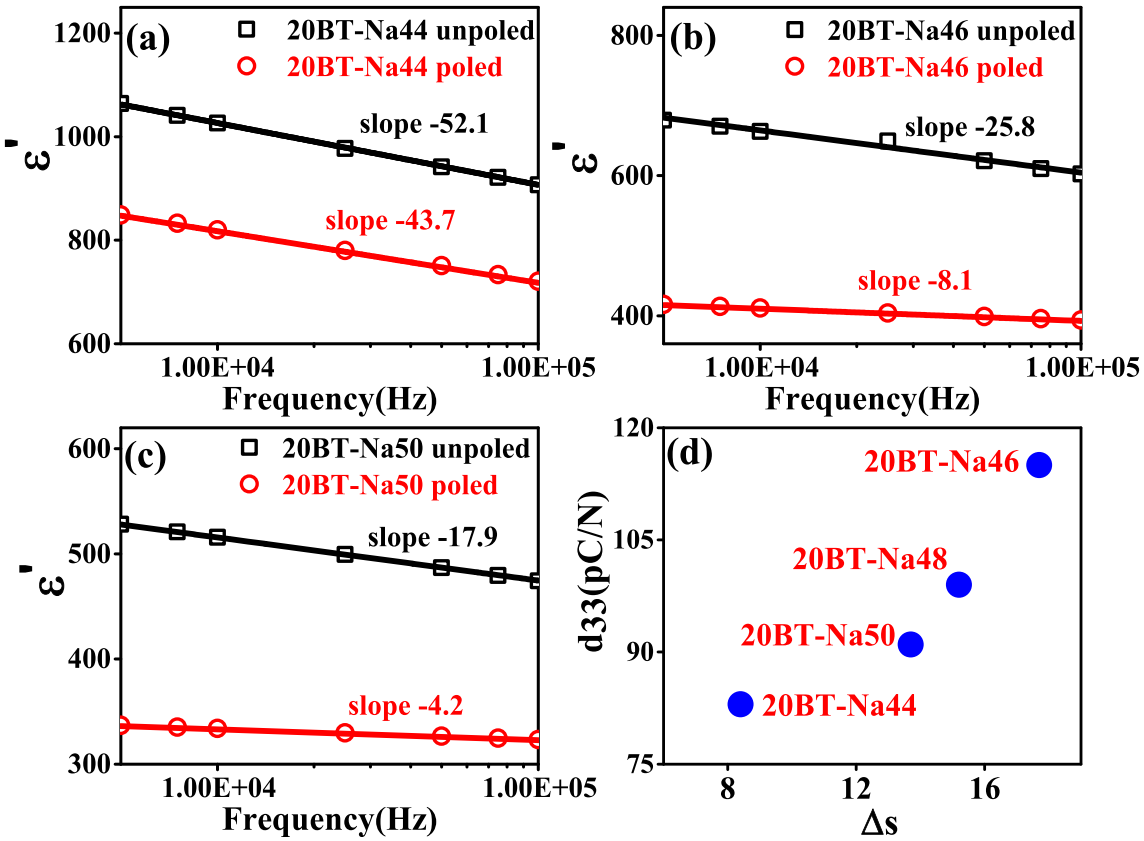

Fig. 10 Dielectric dispersion (permittivity vs ln frequency) plots measured on unpoled and poled (**a**) 20BT–Na44, (**b**) 20BT–Na46, and (**c**) 20BT–Na50 specimens. (**d**) Longitudinal piezoelectric response (d_{33}) as a function of "degree of ordering" (Δs) for Na-deficient compositions of the NBT–20BT series. The measurements were carried out in the frequency range of 10^3–10^5 Hz at room temperature. In (**d**) the error bars are not visible as they are smaller than the data points

Table 5 A-site off-stoichiometric compositions of NBT–20BT along with their electrical resistivity (ρ), piezoresponse (d_{33}), maximum electrostrain (S_{max}), and probable practical utility

Composition	Electrical resistivity (ρ)	Piezoresponse (d_{33})	maximum electrostrain (S_{max})	Practical application
20BT–Na44	0.86×10^9 Ωcm	83 pC/N	0.12%	Actuator, pressure sensor
20BT–Na46	0.87×10^9 Ωcm	115 pC/N	0.14%	Actuator, pressure sensor
20BT–Na48	0.86×10^9 Ωcm	99 pC/N	0.12%	Actuator, pressure sensor
20BT–Na50/20BT–Bi50	0.69×10^9 Ωcm	91 pC/N	0.11%	Actuator, pressure sensor
20BT–Bi52	0.87×10^9 Ωcm	114 pC/N	0.16%	Actuator, pressure sensor
20BT–Bi54	0.88×10^9 Ωcm	102 pC/N	0.14%	Actuator, pressure sensor

tetragonal lattice distortion. Poled specimens of 20BT–Na44, 20BT–Na46, 20BT–Na48, and 20BT–Na50 have a cubic phase fraction of 32%, 25%, 20%, and 15% respectively. The tetragonal lattice distortions of 20BT–Na44, 20BT–Na46, 20BT–Na48, and 20BT–Na50 are 1.8%, 1.9%, 2.0% and 2.1% respectively. The maximum piezoresponse of 115 pC/N is obtained for 20BT–Na46 having an optimized polar-structural heterogeneity of 25% and a tetragonal lattice distortion of 1.9%. Dielectric dispersion studies show that irrespective of the initial polar-structural heterogeneity present in the unpoled matrix, the composition for which the electric field is the most effective in inducing long-range ferroelectric order (degree of ordering), shows the highest piezoresponse. A-site cationic off-stoichiometry could be influencing the

piezoresponse by tuning the polar-structural heterogeneity and ferroelectric lattice distortion via the grain size.

Acknowledgments

Arnab De acknowledges DST, Govt of India for Inspire fellowship. CeNSE, IISc is acknowledged for the SEM-imaging facility.

Declarations

Conflict of interest The authors declared no competing personal or financial interest.

References

1. G.H. Haertling, J. Am. Ceram. Soc. **82**, 797 (1999)
2. A. Arnau, *Piezoelectric Transducers and Applications* (Springer, Berlin, 2004).
3. J.G. Gualtieri, J.A. Kosinski, A. Ballato, IEEE Trans. Ultrason. Ferroelectr. Freq. Control **41**, 53 (1994)
4. C. Lu, A.W. Czanderna, *Applications of Piezoelectric Quartz Crystal Microbalances* (Elsevier, Amsterdam, 2012).
5. G. Wang, J. Li, X. Zhang, Z. Fan, F. Yang, A. Feteira, D. Zhou, D.C. Sinclair, T. Ma, X. Tan, D. Wang, I.M. Reaney, Energy Environ. Sci. **12**, 582 (2019)
6. B. Jaffe, W.R. Cook, H. Jaffe, The piezoelectric effect in ceramics. *Piezoelectric Ceramics*, pp. 7–21, (1971)
7. D.A. Hall, A. Steuwer, B. Cherdhirunkorn, T. Mori, P.J. Withers, Acta Mater. **54**, 3075 (2006)
8. D.A. Hall, A. Steuwer, B. Cherdhirunkorn, T. Mori, P.J. Withers, J. Appl. Phys. **96**, 4245 (2004)
9. N. Kumar, D.K. Khatua, B. Mahale, R. Ranjan, Phys. Rev. B **97**, 1 (2018)
10. E.C. Directive, Off. J. Eur. Union L **197**, 38 (2012)
11. E.C. Directive, Off J. Eur. Union L **37**,13 (2003)
12. J. Rödel, W. Jo, K.T.P. Seifert, E.M. Anton, T. Granzow, D. Damjanovic, J. Am. Ceram. Soc. **92**, 1153 (2009)
13. J. Wu, J. Appl. Phys. **127**, 190901 (2020)
14. J. Rödel, J.F. Li, MRS Bull. **43**, 576 (2018)
15. P.K. Panda, B. Sahoo, Ferroelectrics **474**, 128 (2015)
16. I. Coondoo, N. Panwar, A. Kholkin, J. Adv. Dielectr. **03**, 1330002 (2013)
17. T.R. Shrout, S.J. Zhang, J. Electroceram. **19**, 111 (2007)
18. Y. Hiruma, Y. Imai, Y. Watanabe, H. Nagata, T. Takenaka, Appl. Phys. Lett. **92**, 2 (2008)
19. D.K. Khatua, A. Senyshyn, R. Ranjan, Phys. Rev. B **93**, 1 (2016)
20. J. Rödel, K.G. Webber, R. Dittmer, W. Jo, M. Kimura, D. Damjanovic, J. Eur. Ceram. Soc. **35**, 1659 (2015)
21. S.T. Zhang, A.B. Kounga, E. Aulbach, H. Ehrenberg, J. Rödel, Appl. Phys. Lett. **91**, 2 (2007)
22. S.T. Zhang, A.B. Kounga, E. Aulbach, T. Granzow, W. Jo, H.J. Kleebe, J. Rödel, J. Appl. Phys. **103**, 1 (2008)
23. A.R. Paterson, H. Nagata, X. Tan, J.E. Daniels, M. Hinterstein, R. Ranjan, P.B. Groszewicz, W. Jo, J.L. Jones, MRS Bull. **43**, 600 (2018)
24. T. Takenaka, K. Maruyama, K. Sakata, Jpn. J. Appl. Phys. **30**, 2236 (1991)
25. Y.S. Sung, J.M. Kim, J.H. Cho, T.K. Song, M.H. Kim, T.G. Park, Appl. Phys. Lett. **96**, 1 (2010)
26. K. Datta, K. Roleder, P.A. Thomas, J. Appl. Phys. **106**, 123512 (2009)
27. K. Datta, P.A. Thomas, K. Roleder, Phys. Rev. B **82**, 1 (2010)
28. R. Garg, B.N. Rao, A. Senyshyn, P.S.R. Krishna, R. Ranjan, Phys. Rev. B **88**, 1 (2013)
29. R. Ranjan, A. Dviwedi, Solid State Commun. **135**, 394 (2005)
30. J.E. Daniels, W. Jo, J. Rödel, J.L. Jones, Appl. Phys. Lett. **95**, 2007 (2009)
31. I. Levin, I.M. Reaney, Adv. Funct. Mater. **22**, 3445 (2012)
32. P.B. Groszewicz, M. Gröting, H. Breitzke, W. Jo, K. Albe, G. Buntkowsky, J. Rödel, Sci. Rep. **6**, 1 (2016)
33. P.B. Groszewicz, H. Breitzke, R. Dittmer, E. Sapper, W. Jo, G. Buntkowsky, J. Rödel, Phys. Rev. B **90**, 1 (2014)
34. R. Garg, B. Narayana Rao, A. Senyshyn, R. Ranjan, J. Appl. Phys. **114**, 2 (2013)
35. C. Ma, H. Guo, X. Tan, Adv. Funct. Mater. **23**, 5261 (2013)
36. W. Jo, S. Schaab, E. Sapper, L.A. Schmitt, H.J. Kleebe, A.J. Bell, J. Rödel, J. Appl. Phys. **110**, 074106 (2011)
37. G.A. Smolenskii, V.A. Isupov, A.I. Agranovskaya, S.N. Popov, Sov. Phys. Solid State **2**, 2584 (1961)
38. E. Aksel, J.S. Forrester, J.L. Jones, P.A. Thomas, K. Page, M.R. Suchomel, Appl. Phys. Lett. **98**, 1 (2011)
39. B.N. Rao, R. Ranjan, Phys. Rev. B **86**, 3 (2012)
40. T.M. Usher, I. Levin, J.E. Daniels, J.L. Jones, Sci. Rep. **5**, 1 (2015)
41. A.M. Balagurov, E.Y. Koroleva, A.A. Naberezhnov, V.P. Sakhnenko, B.N. Savenko, N.V. Ter-Oganessian, S.B. Vakhrushev, Phase Transit. **79**, 163 (2006)
42. S. Gorfman, P.A. Thomas, J. Appl. Crystallogr. **43**, 1409 (2010)
43. B.N. Rao, M. Avdeev, B. Kennedy, R. Ranjan, Phys. Rev. B **92**, 1 (2015)
44. B.N. Rao, D.K. Khatua, R. Garg, A. Senyshyn, R. Ranjan, Phys. Rev. B **91**, 1 (2015)
45. A. Mishra, D.K. Khatua, A. De, B. Majumdar, T. Frömling, R. Ranjan, Acta Mater. **164**, 761 (2019)

46. A. Mishra, D.K. Khatua, A. De, R. Ranjan, J. Appl. Phys. **125**, 214101 (2019)
47. Y.S. Sung, J.M. Kim, J.H. Cho, T.K. Song, M.H. Kim, T.G. Park, Appl. Phys. Lett. **98**, 2009 (2011)
48. Y.S. Sung, J.M. Kim, J.H. Cho, T.K. Song, M.H. Kim, H.H. Chong, T.G. Park, D. Do, S.S. Kim, Appl. Phys. Lett. **96**, 3 (2010)
49. M.D. Abràmoff, P.J. Magalhães, S.J. Ram, Biophotonics Int. **11**, 36 (2004)
50. C.A. Schneider, W.S. Rasband, K.W. Eliceiri, Nat. Methods **9**, 671 (2012)
51. H. Ogihara, C.A. Randall, S. Trolier-Mckinstry, J. Am. Ceram. Soc. **92**, 1719 (2009)
52. J. Rodríguez-Carvajal, FullProf. (CEA/Saclay, France, 2001)
53. T. Durga Rao, R. Ranjith, S. Asthana, J. Appl. Phys. **115**, 124110 (2014)
54. T. Choi, Y. Horibe, H.T. Yi, Y.J. Choi, W. Wu, S.W. Cheong, Nat. Mater. **9**, 253 (2010)
55. M. Li, M.J. Pietrowski, R.A. De Souza, H. Zhang, I.M. Reaney, S.N. Cook, J.A. Kilner, D.C. Sinclair, Nat. Mater. **13**, 31 (2014)
56. L. Koch, S. Steiner, K.C. Meyer, I.T. Seo, K. Albe, T. Frömling, J. Mater. Chem. C **5**, 8958 (2017)
57. T. Frömling, S. Steiner, A. Ayrikyan, D. Bremecker, M. Dürrschnabel, L. Molina-Luna, H.J. Kleebe, H. Hutter, K.G. Webber, M. Acosta, J. Mater. Chem. C **6**, 738 (2018)
58. J. Carter, E. Aksel, T. Iamsasri, J.S. Forrester, J. Chen, J.L. Jones, Appl. Phys. Lett. **104**, 3 (2014)
59. R. Pandey, B. Narayan, D.K. Khatua, S. Tyagi, A. Mostaed, M. Abebe, V. Sathe, I.M. Reaney, R. Ranjan, Phys. Rev. B **97**, 1 (2018)
60. V. Dorcet, G. Trolliard, Acta Mater. **56**, 1753 (2008)
61. R. Beanland, P.A. Thomas, Phys. Rev. B **89**, 1 (2014)
62. D.K. Khatua, A. Mishra, N. Kumar, G. Das Adhikary, U. Shankar, B. Majumdar, R. Ranjan, Acta Mater. **179**, 49 (2019)
63. G.A. Samara, J. Phys. Condens. Matter **15**, R367–R411 (2003)
64. N. Kumar, A. Mishra, A. De, U. Shankar, R. Ranjan, J. Phys. D **53**, 1 (2020)
65. G. Abebe, G. Jafo, G. Das Adhikary, A. De, R. Ranjan, A. Mishra, SN Appl. Sci. **2**, 1–18 (2020)
66. D.K. Khatua, A. Kalaskar, R. Ranjan, Phys. Rev. Lett. **116**, 117601 (2016)
67. B.N. Rao, L. Olivi, V. Sathe, R. Ranjan, Phys. Rev. B **93**, 1 (2016)
68. B.N. Rao, A. Senyshyn, L. Olivi, V. Sathe, R. Ranjan, J. Eur. Ceram. Soc. **36**, 1961 (2016)
69. D.K. Khatua, T. Mehrotra, A. Mishra, B. Majumdar, A. Senyshyn, R. Ranjan, Acta Mater. **134**, 177 (2017)
70. M. Muthuramalingam, D.E. Jain Ruth, M. Veera Gajendra Babu, N. Ponpandian, D. Mangalaraj, B. Sundarakannan, Scr. Mater. **112**, 58 (2016)
71. M. Spreitzer, M. Valant, D. Suvorov, J. Mater. Chem. **17**, 185 (2007)
72. M. Veera Gajendra Babu, B. Bagyalakshmi, D. Pathinettam Padiyan, Y. Ren, B. Sundarakannan, Scr. Mater. **141**, 67 (2017)
73. X. Liu, S. Xue, F. Wang, J. Zhai, B. Shen, Acta Mater. **164**, 12 (2019)
74. S. Bhandari, N. Sinha, G. Ray, B. Kumar, Scr. Mater. **89**, 61 (2014)
75. A. Mishra, D.K. Khatua, G. Das Adhikary, N. Kumar, U. Shankar, R. Ranjan, J. Adv. Dielectr. **9**, 1 (2019)
76. Y.R. Zhang, J.F. Li, B.P. Zhang, J. Am. Ceram. Soc. **91**, 2716 (2008)
77. M.V.G. Babu, B. Bagyalakshmi, L. Venkidu, B. Sundarakannan, Ceram. Int. **43**, 12599 (2017)
78. F. Li, D. Lin, Z. Chen, Z. Cheng, J. Wang, C. Li, Z. Xu, Q. Huang, X. Liao, L.Q. Chen, T.R. Shrout, S. Zhang, Nat. Mater. **17**, 349 (2018)
79. B. Narayan, J.S. Malhotra, R. Pandey, K. Yaddanapudi, P. Nukala, B. Dkhil, A. Senyshyn, R. Ranjan, Nat. Mater. **17**, 427 (2018)
80. A. Mishra , B. Majumdar, R. Ranjan, J. Eur. Ceram. Soc. **37**(6), 2379–84 (2017)

Publisher's Note Springer Nature remains neutral with regard to jurisdictional claims in published maps and institutional affiliations.